ACS Photonics

Letter

Cite This: ACS Photonics 2018, 5, 2724−2729

Mode-Hopping Phenomena in the InGaN-Based Core−Shell Nanorod Array Collective Lasing

Chia-Yen Huang,*[†] Tzu-Ying Tai,[†] Jing-Jie Lin,[†] Tsu-Chi Chang,[†] Che-Yu Liu,[†] Tien-Chang Lu,[†] Yuh-Renn Wu,[‡] and Hao-Chung Kuo[†]

[†]Department of Photonics and Institute of Electro-Optical Engineering, College of Electrical and Computer Engineering, National Chiao Tung University, 1001 Ta Hsueh Road, Hsinchu 30010, Taiwan

[‡]Graduate Institute of Photonics and Optoelectronics and Department of Electrical Engineering, National Taiwan University, No. 1, Sec. 4, Roosevelt Road, Taipei 10617, Taiwan

Supporting Information

ABSTRACT: A two-dimensional monolithic InGaN-based core−shell nanorod array was excited under a varying temperature. We observed an abrupt dominant mode hopping from 3.29 to 3.41 eV in the collective lasing as the temperature decreased from T = 240 to 225 K. Photoluminescence under a near-threshold pumping density revealed the splitting of spontaneous emission between the core and the shell with a decreasing temperature. The bandgap evolution of GaN and InGaN showed opposite trends due to the interaction of temperature effects and bandgap renormalization effects. Theoretical simulation revealed the differences of gain spectra evolution between room temperature and low temperature due to the difference in the carrier dynamics. In the optically coupled nanorod array, the dominant lasing mode was not only determined by its structure, but also strongly influenced by external operating conditions. Rather than singular microcavity lasers, the coupled nanorod array demonstrated a broader parameter space for on-chip wavelength manipulation.

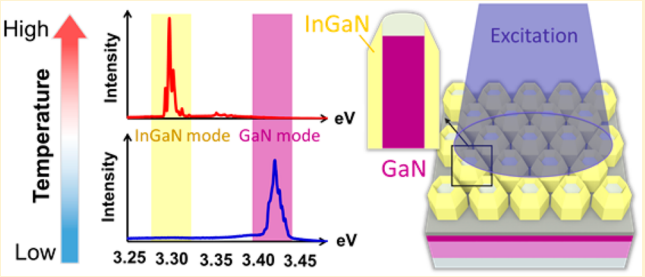

KEYWORDS: *GaN, InGaN, core−shell, microcavity, collective lasing, mode hopping*

Microcavity lasers have many important characteristics such as compact volume, ultralow threshold pumping level and very fast speed, which are attractive for future photon-based information technologies.[1−5] InGaN-based microcavity lasers and nanolasers also attracted much attention for its potential for new technology development in UV−visible spectral range. Nitride-based nanowire lasers were first demonstrated in Fabry-Pérot type cavities with either pure nanowire or core−shell structures.[6−9] Even though the decent performance of nanowire lasers, the delicate manipulation process brought strong challenges for a large-area integration with other devices. Whispering gallery mode (WGM) lasers possessed an ultrahigh quality factor (Q-factor) and can be fabricated monolithically. Nitride-based WGM lasers in suspended microdisk cavities have been demonstrated in a wide spectral region from blue to deep ultraviolet.[10−13] The reported diameters of microdisk ranged from few microns to tens of microns in order to suppress the scattering loss through the high-curvature perimeter, which would deteriorate the Q-factor and cause an enhanced threshold. Previous researches in ZnO-based hexagon WGM lasers observed that the threshold pumping densities were inverse proportional to the hexagon width.[14,15] To improve the Q-factor, we formed the submicron hexagon cavity via a pattern-and-regrowth process to suppress the scattering loss via edge roughness.[16] Theoretical simulations have predicted a significant reduction of threshold pumping density by critical coupling between adjacent microdisks by forming "photonic molecules".[17,18] In analogy, we put the nanorod closely to form a two-dimensional periodic array. We have confirmed the collective WGM lasing in such array with a decent Q-factor (∼1940), where each cavity was in submicron level and the threshold pumping density was as low as 140 kW/cm^2.[16] The excitation-area-dependent lasing behavior in the nanorod array was explained by different coupling strength among the different cavity modes. The dominant lasing mode "hopped" from short-wavelength modes to long-wavelength modes as the number of excited nanorods increased. In this study, we revealed another temperature-induced mode-hopping phenomena due to the evolution of gain spectrum. A semiquantitative model will be delivered to generalize the dominant mode selection in the coupled core−shell nanorod periodic array.

Figure 1a was the scanning electron microscope (SEM) image of the hexagon cavity from the top. The hexagon was surrounded by m-planes, whose diagonal was estimated to be 850 nm with a 50 nm corner-to-corner distance. Figure 1b−d

Received: April 12, 2018
Published: June 19, 2018

DOI: 10.1021/acsphotonics.8b00471
ACS Photonics 2018, 5, 2724−2729

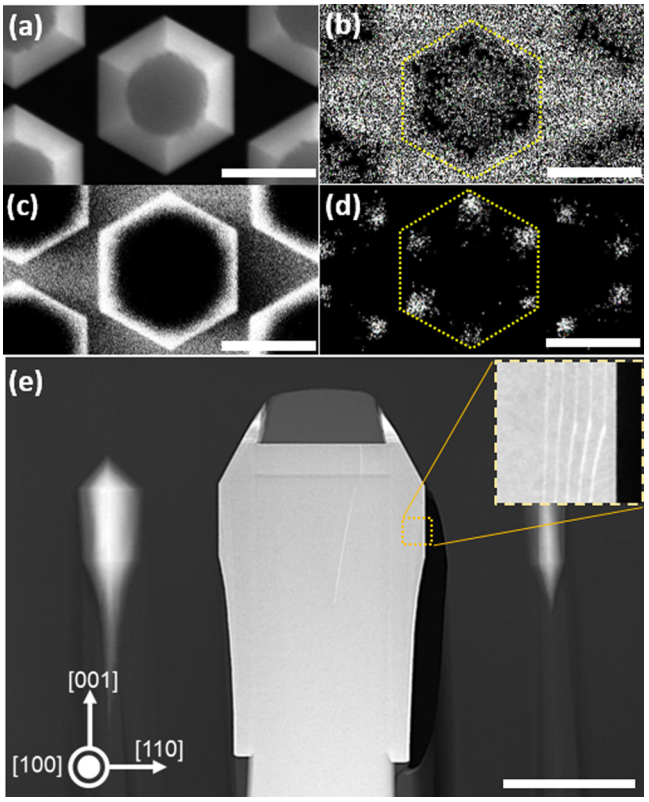

Figure 1. (a) SEM top view image and the monochromatic CL image under (b) λ = 365 nm, (c) λ = 376 nm, and (d) λ = 410 nm of the GaN-InGaN core−shell array. The yellow dashed lines in (b) and (d) were visual guideline of the cavity perimeter. (e) Cross-sectional STEM image from the [100] direction. Inset is the magnified image in the shell region. All white bars represented 500 nm in the figure.

was the monochromatic cathodoluminescence (CL) image under λ= 365 nm ($h\nu$ = 3.40 eV), 376 nm ($h\nu$ = 3.30 eV), and 410 nm ($h\nu$ = 3.03 eV), respectively. The fabrication process could be found in the Supporting Information. The 365 nm emission originated from GaN materials in the core region and the field, and the 376 nm emission came from the InGaN-GaN multiple-quantum-well (MQW) in the shell region. The 410 nm emission appeared on the six corners of the hexagon cavity. According to the CL images and scanning transmission electron microscope (STEM) image in Figure 1 (e), the 410 nm emission is attributed to the parasitic In cluster at the edges of the top passivation layer during regrowth. Because the In clusters did not lie on the same horizontal plane with the major core−shell structure, its influence on the WGM lasing shall be minimal. Therefore, we decoupled their contribution in photoluminescence (PL) for modeling.

The samples was mounted on a temperature-controlled module and excited by 355 nm Nd:YVO_4 pulse solid-state lasers. See Supporting Information for the micro-PL setup. We chose a relatively large spot size ($D \sim 100\ \mu$m) to excite tens of thousands of nanorods simultaneously to study the collective lasing. Figure 2a was the temperature-dependent lasing spectrum under constant pumping power P = 300 kW/cm^2. Under room temperature, dominant peaks located near 3.3 eV. The fine peak splitting in the vicinal spectral region was attributed to the formation of supermodes due to rod-to-rod mode interaction.[19,20] As the temperature decreased from 300 to 195 K, the lasing peak around 3.3 eV gradually diminished, while those near 3.4 eV arose. For brevity, we named the lasing modes residing in the spectral range from 3.28 to 3.32 eV as "InGaN modes", and those in the range from 3.35 to 3.41 eV as "GaN modes" in the following text due to its corresponding principle gain medium. In other words, the dominant mode hopped from InGaN modes to GaN modes as the temperature decreased from T = 255 to 240 K. Figure 2b,c was the L−L

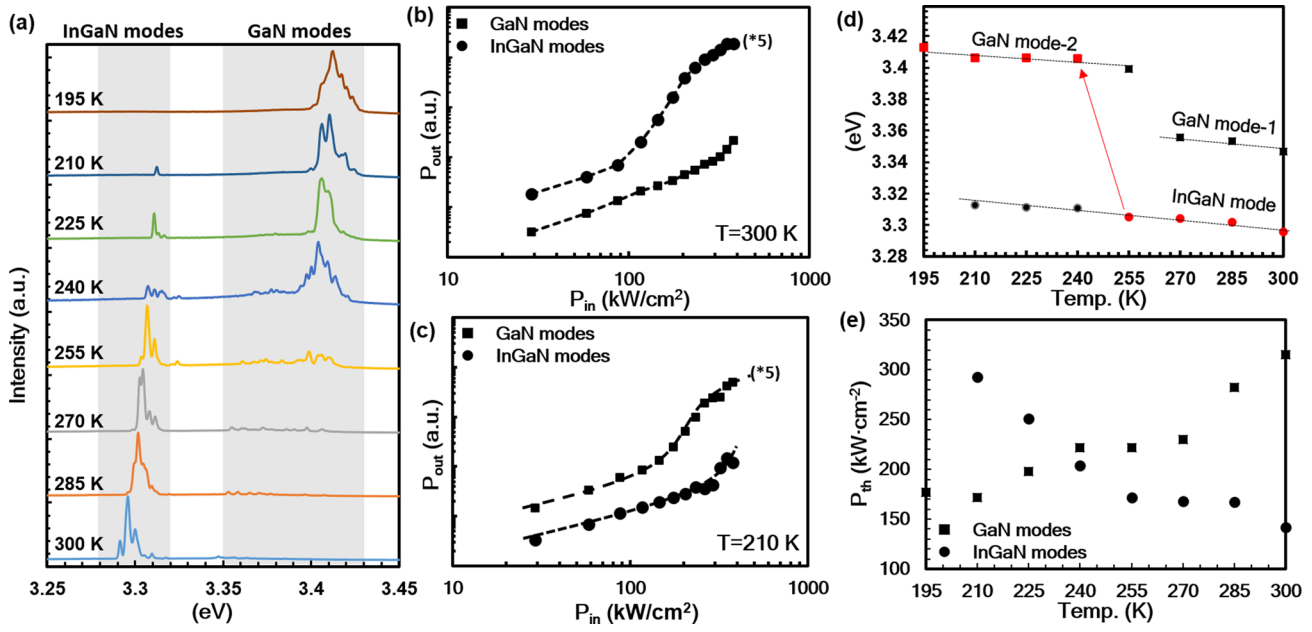

Figure 2. (a) Temperature-dependent lasing spectrum under P = 300 kW/cm^2 and the definition of GaN modes and InGaN modes. The light−light curves of the strongest peak in each mode under (b) T = 300 K and (c) 210 K. The intensity of the lower-threshold mode was intentionally shifted 5 times for plot clarity. (d) Dominant lasing mode among each group under different ambient temperatures. The overall strongest peak was marked in red. (e) Extracted threshold pumping densities under different temperatures.

DOI: 10.1021/acsphotonics.8b00471
ACS Photonics 2018, 5, 2724−2729

curves of the strongest peak in each mode under 300 and 210 K, respectively. Under 300 K, 3.29 eV lasing emerged under a threshold pumping density (P_{th}) of 140 kW/cm^2, while GaN modes lasing (~3.35 eV) took place under $P_{th} \sim 300$ kW/cm^2. Under 210 K, the 3.41 eV GaN modes lasing became the earliest one with a $P_{th} \sim 170$ kW/cm^2 instead. InGaN modes lasing was delayed to $P_{th} = 280$ kW/cm^2, and the energy was blue-shifted from 3.29 to 3.31 eV. The same power-dependent PL measurement and L−L curve analysis was conducted from $T = 195$ to 300 K. Figure 2d,e summarized the strongest lasing peak energy under $P \sim 300$ kW/cm^2 and their corresponding P_{th}s. The smooth blue shift of dominant InGaN mode was attributed to the shift of cavity resonant wavelength due to the temperature-dependent refractive indices of nitrides.[21,22] Therefore, the abrupt mode-hopping within GaN modes from $T = 270$ to 255 K indicated the existence of two distinguishable cavity modes. No matter the major mode-hopping of the strongest peak (marked red in Figure 2d) or the minor hopping among GaN modes, they were all influenced by the gain spectrum evolution with temperature. In the following section, a semiquantitative theoretical simulation was performed to illustrate the carrier dynamics in the core−shell structure and its influences on the gain spectrum.

A one-dimensional shell−core−shell multilayer model was built to simulate the gain spectrum under a high excitation level, as illustrated in Figure 3a. The input thicknesses of shell layers (W_{shell}) adopted from STEM characterization, which consisted of five pairs of InGaN/GaN multiple-quantum-wells. Since the calculation of overall material gain and PL emission was related to the area, the input core width for simulation ($W_{c,sim}$) was revised to simulate the actual area ratio by

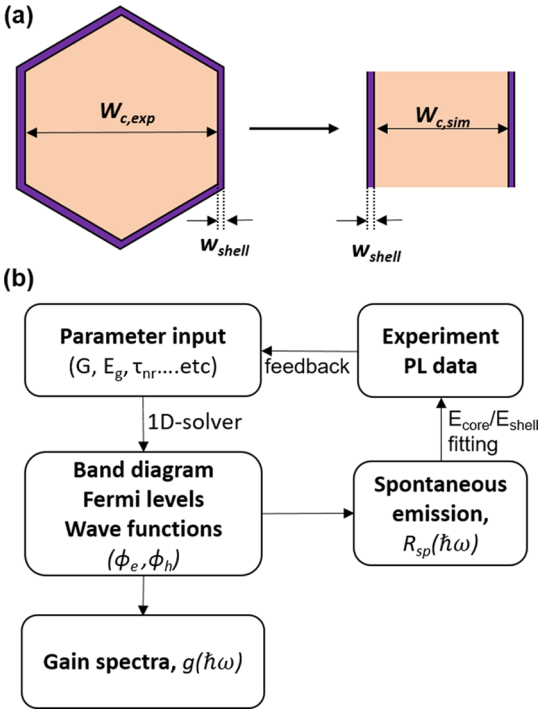

Figure 3. (a) Schematic illustration of constructing the one-dimensional model (right) from the two-dimensional case (left). (b) Flowchart of PL modeling and gain spectra simulation.

$$\frac{W_{c,sim}}{2W_{shell}} = \frac{\text{area of core}}{\text{area of shell}} \sim \frac{6 \times \frac{\sqrt{3}}{4} \times \left(\frac{W_{c,exp}}{\sqrt{3}}\right)^2}{6 \times \frac{W_{c,exp}}{\sqrt{3}} \times W_{shell}} = \frac{W_{c,exp}}{4W_{shell}} \quad (1)$$

which yielded

$$W_{c,sim} = \frac{W_{c,exp}}{2} \quad (2)$$

where $W_{c,exp}$ was the core width extracted from STEM characterizations. The average carrier generation rate (G) under optical pumping density P was calculated by

$$G = \frac{P\alpha}{h\nu} \quad (3)$$

where α is the absorption coefficient of materials. Under 355 nm ($h\nu \sim 3.5$ eV) excitation, the α of GaN and InGaN layer was both assumed to be the same ($\alpha_{GaN} = \alpha_{InGaN} = 8 \times 10^4$ cm^{-1}) because the In composition is relatively low.[23] The values of materials parameters and transport parameters such as radiative recombination rate constants (B), Auger coefficient (C), carrier motilities, and line shape broadening parameter adopted either from literatures or estimated by Vegard's Law. The schematic modeling and simulation procedure were illustrated in Figure 3b. Structure parameters were input to a drift-diffusion charge-control numerical solver, which solved Poisson, drift-diffusion, and landscape equations self-consistently.[24] After the equilibrium band diagram with quasi-Fermi levels (E_{fn}, E_{fp}) were obtained, the carrier envelope wave functions in the confined direction ($\phi_{e,i}(z)$, $\phi_{h,j}(z)$) and their eigen energy were calculated by solving the Schrodinger equations in the band diagram. Therefore, we can use these results to estimate the PL and gain spectra. The formalism to solve the spontaneous emission rate (R_{sp}) is given by

$$R_{sp}(\hbar\omega) = \frac{e^2 n_r \hbar\omega}{m_0^2 \int_0 c^3 \hbar^2} \sum_{i,j} \frac{N_{2D}}{W} |p_{i,j}|^2 \times \frac{1}{2}\left[1 + \text{erf}\left(\frac{\hbar\omega - E_{ij}}{\sqrt{2}\sigma}\right)\right] f_e f_h \quad (4)$$

where n_r is the refractive index, W is the overall rod width, and N_{2D} is the two-dimensional reduced density of state, which is

$$N_{2D} = \frac{m_r^*}{\pi\hbar^2} \quad (5)$$

m_r^* is the reduced effective mass. $\mathbf{p}_{ij}$ is the momentum matrix element. For electron and hole in the QW, the complete electron and hole wave function can be expressed as

$$\Phi_{e,i} = \phi_i(z) e^{ik_{e,i}\rho} u_c(r) \quad (6)$$

$$\Phi_{h,j} = \phi_j(z) e^{ik_h\rho} u_v(r) \quad (7)$$

where ρ is the lateral direction and u_c and u_v represents the conduction and valence band central cell states, respectively. The momentum matrix element can be expressed as

$$\mathbf{p}_{ij} = \langle \Phi_{e,i} | (-i\hbar\nabla) | \Phi_{h_j} \rangle = \langle \phi_{e,i}(z) | \phi_{h,j}(z) \rangle \int e^{i(k_e - k_h)\rho} \langle u_c | (-i\hbar\nabla) | u_v \rangle d^2\rho \quad (8)$$

Since $k_e \sim k_h$ and $e^{i(k_e - k_h)\rho} = 1$, we obtain

$$\mathbf{p}_{ij} = \langle \phi_{e,i}(z) | \phi_{h,j}(z) \rangle \langle u_c | \mathbf{p} | u_v \rangle \quad (9)$$

The erf(x) is the error function after the integration of Gaussian broadening line-shape functions. E_{ij} is the transition

DOI: 10.1021/acsphotonics.8b00471
ACS Photonics 2018, 5, 2724−2729

energy between $\phi_{e,i}$ and $\phi_{h,j}$. σ is the inhomogeneous Gaussian broadening coefficient, which was set to be 30 meV according to previous modeling works on InGaN-based laser diodes.[25] f_e and f_h are the Fermi−Dirac distribution function of electrons and holes, respectively.

To calculate the gain, the formalism becomes

$$g(\hbar\omega) = \frac{\pi e^2 \hbar}{n_r c m_0^2 \int_0(\hbar\omega)} \sum_{i,j} \frac{N_{2D}}{W} |p_{i,j}|^2 \times \frac{1}{2}\left[1 + \mathrm{erf}\left(\frac{\hbar\omega - E_{ij}}{\sqrt{2}\sigma}\right)\right] \times (f_e + f_h - 1) \quad (10)$$

Because the direct measurement of gain spectrum in nanorods is challenging, we proposed to simulate the gain spectrum by modeling the PL emission under near-threshold pumping condition. The simulated PL spectrum were then decomposed into two Gaussian function, representing to the PL emission from core region and shell region, respectively. Similar Gaussian decomposition procedure was conducted to experimental data as well. After peak energies in simulation were best fitted to experiment data, the gain spectrum under the near threshold condition was acquired simultaneously. The major free-varying variables during modeling were the band gaps of GaN ($E_{g,GaN}$) and InGaN ($E_{g,InGaN}$) because they were highly dependent on the temperature and plasma densities.[21,26] Prior to the detailed analysis, please be noted that this model might not be applicable for all nanowire lasers. For example, if the nanowire dimension is in the same order of carrier wavelength, the core region shall not be treated as bulk, and the density of state of the quantum well will be no more a constant as depicted in eq 5. Besides, the potential strong coupling between the microcavity mode and carriers (a.k.a. polaritons) also fails the transport models. Fortunately, the rod size in this study in the order of few hundred nanometers, so the numerical solver with conventional transport models could be trusted.

Figure 4a were the Gaussian decomposition of PL under $P \sim 110$ kW/cm^2 under different temperatures. Since the emission came from core, shell, and top-corner regions, the PL were fitted with three Gaussian distribution functions. The contribution from top-corner was subtracted during PL modeling. The extracted peak energy with temperatures were plotted in Figure 4b. As temperature decreased from 300 to 210 K, the emission peak energy from core (E_{core}) shifted from 3.366 to 3.401 eV. The bandgap blueshift with reducing temperature were commonly observed in GaN. However, the extracted peak energies were lower than the fundamental $E_{g,GaN}$, which is around 3.42 eV under room temperature and 3.45 eV under 210 K in the ref 21. The difference could be attributed to the bandgap renormalization effect under a strong excitation. In comparison, the peak energies from shell region were not as sensitive to temperature as those of GaN were. We attributed the insensitivity due to the competing mechanism between the temperature effect and the bandgap renormalization effect. Under a low temperature, the Fermi−Dirac distribution becomes more abrupt and the low energy states are more probable to be filled. Therefore, more excess carriers populated in the quantum wells under the same excitation level, which also enhanced the bandgap renormalization effect of InGaN. The overall emission was also broadened due to the more prominent peak, which might explain the enhanced threshold value under a lower temperature.

After the iterative modeling, the best-fitted $E_{g,GaN}$ and $E_{g,InGaN}$ was estimated to be 3.345 and 3.190 eV under 300 K and was 3.392 and 3.154 eV under 210 K, respectively. The variation trend was consistent with those in Figure 4b. The best-fitted band diagram, carrier distribution, and R_{sp} could be found in the Supporting Information. According to the simulation result, the electron density in the core region under T = 300 K was estimated to be 9.6×10^{18} cm^{-3}. In ref 26, such plasma density yielded a ∼85 meV energy bandgap shrinkage, which also matched the difference between the fundamental bandgap and the best-fitted $E_{g,GaN}$. Similar trend was also observed under T = 210 K. Therefore, we believe the modeling algorithm is physically sound and self-consistent. Based on these modeled bandgaps, the gain spectra were calculated in the proximal pumping densities. Figure 5 illustrated the power-dependent gain spectra with equi-gain contours (black dashed line) under 300 and 210 K. While T = 300 K, the gain contribution from the core and the shell could not be distinguished due to the closeness of $E_{g,GaN}$ and $E_{g,InGaN}$. Under the threshold condition (P_{th} = 140 kW/cm^2, white dashed line in Figure 5a), the maximum gain was at $\hbar\omega$ = 3.29 eV, while $g(\hbar\omega)$ was still less than zero for $\hbar\omega$ > 3.35 eV. As a result, the InGaN modes lasing prevailed. It is worth noticing that the carrier recombination via stimulated emission was not yet included in the model, so the above-threshold gain spectra simulation will not be quantitatively accurate. However, we could still infer that the low energy modes among the GaN modes would be activated first as the pumping power increased under room temperature. On the contrary, the gain spectra under 210 K evolved in a different manner. Because the excess

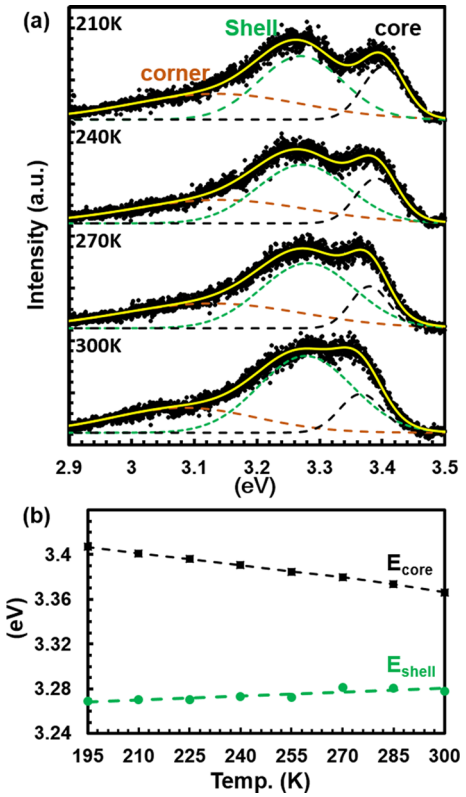

Figure 4. (a) Decomposition of PL spectra under P = 110 kW/cm^2 with three Gaussian functions. According to its peak energy position, three emission envelopes were assigned to be from the core (black dashed lines), shell (green dashed lines), and top corner (brown dashed lines) regions. The yellow solid lines were accumulation of three Gaussian function. (b) Temperature dependence of peak energy position from the core and shell emissions.

DOI: 10.1021/acsphotonics.8b00471
ACS Photonics 2018, 5, 2724−2729

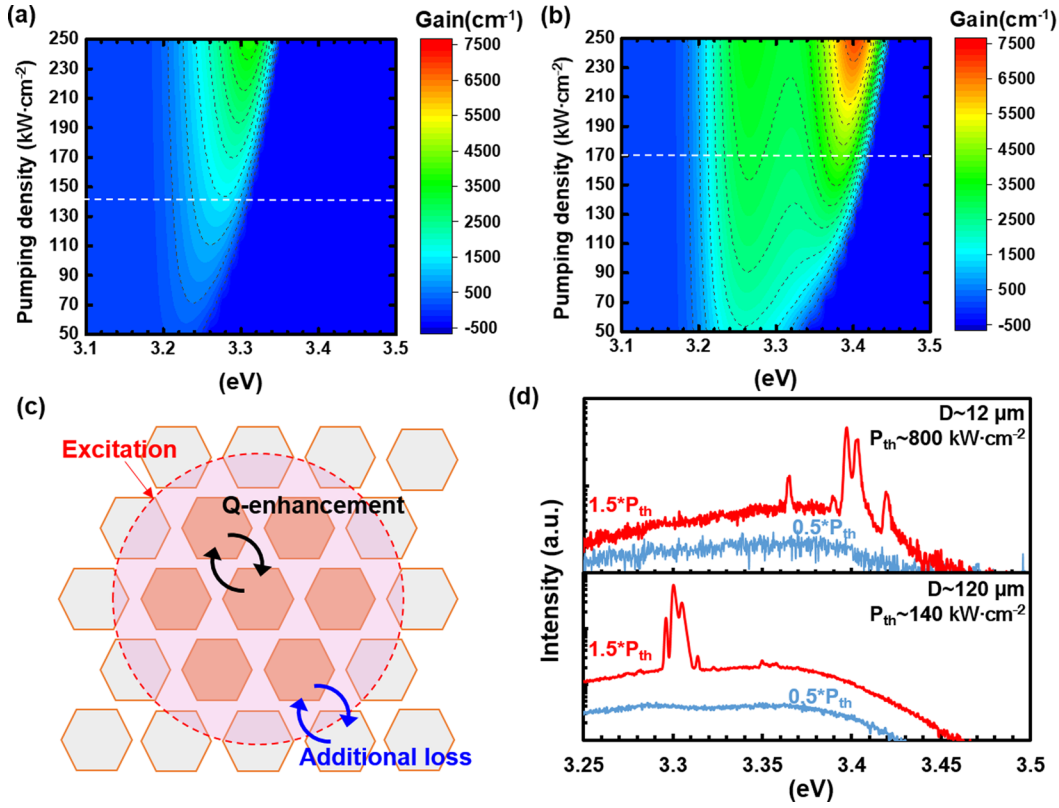

Figure 5. Color-mapped gain spectra simulation under various pumping density level with (a) T = 300 and (b) 210 K. White-dashed lines represented the corresponding threshold pumping level. (c) Schematic illustration of mode coupling in the center or the peripheral region of excitation. (d) Lasing spectra under room temperature with a different diameter (D) of excitation area.

carriers populated the InGaN MQW more densely under a low temperature, the $g(\hbar\omega < 3.30$ eV) still dominated under a relatively low P ($P < 100$ kW/cm^2). After most of electronic states in MQW were populated, the gain contribution from MQW started to saturate and a distinguishable shoulder emerged in the high-energy side. Because of the substantial volume of GaN in the core−shell structure, the gain spectra were soon dominated by the GaN materials. Under the near threshold condition of T = 210 K, the maximum of gain took place at E = 3.38 eV instead, which well-explained the prevalence of high-energy GaN modes lasing under a low temperature.

Regardless of the ambient temperature, the local gain maximum always shifts to higher energy under a stronger excitation. Therefore, additional optical loss in the system could also result in the dominant lasing mode hopping due to a higher threshold; for example, coupling the excited nanorod to a lossy media. Because the excitation area was finite, those excited rods in the peripheral region were coupled to unexcited ones, which brought additional optical losses to the system, as depicted in Figure 5c. High energy GaN modes were therefore dominated under a small excitation area due to a stronger edge effect. Figure 5d showed that the dominant mode shifted from 3.3 to 3.4 eV by focusing the laser spot size down to a diameter of 12 μm, while the P_{th} was increased from 140 to 800 kW/cm^2. The gain spectra simulation also provided the excitation-area-dependent collective lasing an alternative explanation besides the different coupling strength among the different cavity modes.

In conclusion, we attributed the temperature-induced mode hopping to the different extent of bandgap renormalization between GaN and InGaN materials within the core−shell structure. The core−shell structure determined the cavity mode and the baseline of gain spectra under excitation. External parameters such as excitation area or coupling strength among rods also determine the final dominant lasing mode because it influenced the threshold pumping density significantly. Therefore, the measure to manipulate the dominant lasing mode in the coupled nanorod arrays is richer rather than that in uncoupled ones. With a careful control in the core−shell structure and the rod arrangement, it is practically achievable to design and manipulate the lasing wavelength in a single monolithic photonics chip in UV−visible spectra region.

■ ASSOCIATED CONTENT

Supporting Information

The Supporting Information is available free of charge on the ACS Publications website at DOI: 10.1021/acsphotonics.8b00471.

Detailed fabrication process, micro-PL measurement setup, modeled band diagrams, carrier distribution, and spontaneous emission rates under T = 300 and 210 K (PDF).

■ AUTHOR INFORMATION

Corresponding Author

*E-mail: yenhuang@nctu.edu.tw.

ORCID

Chia-Yen Huang: 0000-0003-0844-1903

DOI: 10.1021/acsphotonics.8b00471
ACS Photonics 2018, 5, 2724−2729

Notes

The authors declare no competing financial interest.

■ ACKNOWLEDGMENTS

This research was funded by Ministry of Science and Technology (MoST) of Taiwan under the Project Contact No. 106-2221-E-009-119 and No. 105-2221-E-002 -098 -MY3.

■ REFERENCES

(1) Vahala, K. J. Optical microcavities. *Nature* **2003**, *424*, 839−846.
(2) Altug, H.; Englund, D.; Vučković, J. Ultrafast photonic crystal nanocavity laser. *Nat. Phys.* **2006**, *2*, 484−488.
(3) Halioua, Y.; Bazin, A.; Monnier, P.; Karle, T. J.; Roelkens, G.; Sagnes, I.; Raj, R.; Raineri, F. Hybrid III-V semiconductor/silicon nanolaser. *Opt. Express* **2011**, *19*, 9221−9231.
(4) Roelkens, G.; Liu, L.; Liang, D.; Jones, R.; Fang, A.; Koch, B.; Bowers, J. E. III-V/silicon photonics for on-chip and intra-chip optical interconnects. *Laser Photonics Rev.* **2010**, *4*, 751−779.
(5) Liang, D.; Bowers, J. E. Recent progress in lasers on silicon. *Nat. Photonics* **2010**, *4*, 511−517.
(6) Johnson, J. C.; Choi, H. J.; Knutsen, K. P.; Schaller, R. D.; Yang, P.; Saykally, R. J. Single gallium nitride nanowire lasers. *Nat. Mater.* **2002**, *1*, 106−110.
(7) Qian, F.; Li, Y.; Gradečak, S.; Park, H. G.; Dong, Y.; Ding, Y.; Wang, Z. L.; Lieber, C. M. Multi-quantum-well nanowire heterostructures for wavelength-controlled lasers. *Nat. Mater.* **2008**, *7*, 701−706.
(8) Zhao, S.; Liu, X.; Woo, S. Y.; Kang, J.; Botton, G. A.; Mi, Z. An electrically injected AlGaN nanowire laser operating in the ultraviolet-C band. *Appl. Phys. Lett.* **2015**, *107*, 043101.
(9) Li, C.; Wright, J. B.; Liu, S.; Lu, P.; Figiel, J. J.; Leung, B.; Chow, W. W.; Brener, I.; Koleske, D. D.; Luk, T. S.; Feezell, D. F.; Brueck, S. R. J.; Wang, G. T. Nonpolar InGaN/GaN Core−Shell Single Nanowire Lasers. *Nano Lett.* **2017**, *17*, 1049−1055.
(10) Tamboli, A. C.; Haberer, E. D.; Sharma, R.; Lee, K. H.; Nakamura, S.; Hu, E. L. Room-temperature continuous-wave lasing in GaN/InGaN microdisks. *Nat. Photonics* **2007**, *1*, 61−64.
(11) Aharonovich, I.; Niu, N.; Rol, F.; Russell, K. J.; Woolf, A.; El-Ella, H. A. R.; Kappers, M. J.; Oliver, R. A.; Hu, E. L. Controlled tuning of whispering gallery modes of GaN/InGaN microdisk cavities. *Appl. Phys. Lett.* **2011**, *99*, 111111.
(12) Athanasiou, M.; Smith, R.; Liu, B.; Wang, T. Room temperature continuous-wave green lasing from an InGaN microdisk on silicon. *Sci. Rep.* **2015**, *4*, 7250.
(13) Selles, J.; Brimont, C.; Cassabois, G.; Valvin, P.; Guillet, T.; Roland, I.; Zeng, Y.; Checoury, X.; Boucaud, P.; Mexis, M.; Semond, F.; Gayral, B. Deep-UV nitride-on-silicon microdisk lasers. *Sci. Rep.* **2016**, *6*, 21650.
(14) Chen, R.; Ling, B.; Sun, X. W.; Sun, H. D. Room Temperature Excitonic Whispering Gallery Mode Lasing from High-Quality Hexagonal ZnO Microdisks. *Adv. Mater.* **2011**, *23*, 2199−2204.
(15) Dai, J.; Xu, C. X.; Zheng, K.; Lv, C. G.; Cui, Y. P. Whispering gallery-mode lasing in ZnO microrods at room temperature. *Appl. Phys. Lett.* **2009**, *95*, 241110.
(16) Huang, C. Y.; Lin, J. J.; Chang, T. C.; Liu, C. Y.; Tai, T. Y.; Hong, K. B.; Lu, T. C.; Kuo, H. C. Collective Lasing Behavior of Monolithic GaN−InGaN Core−Shell Nanorod Lattice under Room Temperature. *Nano Lett.* **2017**, *17*, 6228−6234.
(17) Boriskina, S. V. Theoretical prediction of a dramatic Q-factor enhancement and degeneracy removal of whispering gallery modes in symmetrical photonic molecules. *Opt. Lett.* **2006**, *31*, 338−340.
(18) Smotrova, E. I.; Nosich, A. I.; Benson, T. M.; Sewell, P. D. Optical coupling of whispering-gallery modes of two identical microdisks and its effect on photonic molecule lasing. *IEEE J. Sel. Top. Quantum Electron.* **2006**, *12*, 78−85.
(19) Bayer, M.; Gutbrod, T.; Reithmaier, J. P.; Forchel, A.; Reinecke, T. L.; Knipp, P. A.; Dremin, A. A.; Kulakovskii, V. D. Optical Modes in Photonic Molecules. *Phys. Rev. Lett.* **1998**, *81*, 2582−2585.
(20) Rakovich, Y. P.; Donegan, J. F.; Gerlach, M.; Bradley, A. L.; Connolly, T. M.; Boland, J. J.; Gaponik, N.; Rogach, A. Fine structure of coupled optical modes in photonic molecules. *Phys. Rev. A: At., Mol., Opt. Phys.* **2004**, *70*, 051801.
(21) Brunner, D.; Angerer, H.; Bustarret, E.; Freudenberg, F.; Höpler, R.; Dimitrov, R.; Ambacher, O.; Stutzmann, M. Optical constants of epitaxial AlGaN films and their temperature dependence. *J. Appl. Phys.* **1997**, *82*, 5090.
(22) Thomas, N.; Evgeni, M. K.; Andreas, R.; Michael, L.; Marius, G. Whispering Gallery Modes in Nanosized Dielectric Resonators with Hexagonal Cross Section. *Phys. Rev. Lett.* **2004**, *93*, 103903.
(23) Muth, J. F.; Lee, J. H.; Shmagin, I. K.; Kolbas, R. M.; Casey, H. C.; Keller, B. P.; Mishra, U. K.; DenBaars, S. P. Absorption coefficient, energy gap, exciton binding energy, and recombination lifetime of GaN obtained from transmission measurements. *Appl. Phys. Lett.* **1997**, *71*, 2572−2574.
(24) Li, C. K.; Piccardo, M.; Lu, L. S.; Mayboroda, S.; Martinelli, L.; Peretti, J.; Speck, J. S.; Weisbuch, C.; Filoche, M.; Wu, Y. R. Localization landscape theory of disorder in semiconductors. III. Application to carrier transport and recombination in light emitting diodes. *Phys. Rev. B: Condens. Matter Mater. Phys.* **2017**, *95*, 144206.
(25) Witzigmann, B.; Laino, V.; Luisier, M.; Schwarz, U. T.; Feicht, G.; Wegscheider, W.; Engl, K.; Furitsch, M.; Leber, A.; Lell, A.; Härle, V. Microscopic analysis of optical gain in InGaN/GaN quantum wells. *Appl. Phys. Lett.* **2006**, *88*, 021104.
(26) Nagai, T.; Inagaki, T. J.; Kanemitsu, Y. Band-gap renormalization in highly excited GaN. *Appl. Phys. Lett.* **2004**, *84*, 1284−1286.

DOI: 10.1021/acsphotonics.8b00471
ACS Photonics 2018, 5, 2724−2729